

Regulation of cell-type-specific transcriptomes by microRNA networks during human brain development

Tomasz J. Nowakowski^{1,2,11*}, Neha Rani^{3,4,11}, Mahdi Golkaram^{5,11}, Hongjun R. Zhou^{1,3,6,11}, Beatriz Alvarado^{1,7}, Kylie Huch^{3,6}, Jay A. West⁸, Anne Leyrat⁸, Alex A. Pollen^{1,9}, Arnold R. Kriegstein^{1,7}, Linda R. Petzold^{5,10} and Kenneth S. Kosik^{1,3,6*}

MicroRNAs (miRNAs) regulate many cellular events during brain development by interacting with hundreds of mRNA transcripts. However, miRNAs operate nonuniformly upon the transcriptional profile with an as yet unknown logic. Shortcomings in defining miRNA–mRNA networks include limited knowledge of in vivo miRNA targets and their abundance in single cells. By combining multiple complementary approaches, high-throughput sequencing of RNA isolated by cross-linking immunoprecipitation with an antibody to AGO2 (AGO2-HITS-CLIP), single-cell profiling and computational analyses using bipartite and coexpression networks, we show that miRNA–mRNA interactions operate as functional modules that often correspond to cell-type identities and undergo dynamic transitions during brain development. These networks are highly dynamic during development and over the course of evolution. One such interaction is between radial-glia-enriched ORC4 and miR-2115, a great-ape-specific miRNA, which appears to control radial glia proliferation rates during human brain development.

Recent studies using single-cell mRNA sequencing (scRNA-seq) to characterize cell-type diversity in tissues have highlighted the need for multimodal analyses of cellular phenotypes by unbiased classification schemas. These analyses are particularly needed for developing systems in which complex gene regulatory networks control orthogonal sources of transcriptional variation, including morphology, physiology, maturation, differentiation, and spatial position^{1–4}. Although mRNA expression levels can be used directly to define putative cell types, unbiased clustering methods to infer cell identities and to determine the boundaries of these identities require either prior knowledge or additional modalities. MicroRNAs (miRNAs) form an inherently complex network of interactions that can serve as an additional feature of cellular identity^{5,6} with important implications for protein expression. miRNAs have a role in fine-tuning signaling pathways related to corticogenesis, and their altered expression is associated with many neurological disorders (reviewed in ref. 7). Changes in miRNA expression patterns that are often large in magnitude occur as defining decision nodes during cell differentiation⁶. This suggests that their cell-type-specific abundance is an important parameter in cell-type identity and provides insights beyond cell-type classification into the dynamic regulation of differentiation. The greater numbers of miRNA encoded in the genome as a function of organismal complexity suggests that the emergence of novel cell types in the primate brain may be associated with increased numbers of cell-type-specific miRNAs in the brain. Previous studies ablating miRNA-processing enzyme Dicer1 emphasize pleiotropic roles for this pathway

related to tissue specificity, anatomical and cellular compartments, evolutionary relationships, developmental time points and even specific cell types^{7–12}, but the underlying framework for these differences is poorly understood. Profiling of miRNA abundance in developing human brain tissue samples has suggested that miRNA expression is developmentally regulated¹³, but these studies have distinguished neither cell-type-specific patterns of miRNA abundance nor dynamic cell-fate transitions during development at the single-cell level. To characterize in vivo miRNA–mRNA interactions during human brain development and to contextualize these networks in the framework of developmental transitions and cell identity, we leveraged three complementary data sets: high-throughput sequencing of RNA isolated by cross-linking immunoprecipitation¹⁴ with an antibody to AGO2 (AGO2-HITS-CLIP) data, simultaneous single-cell profiling data of mRNAs and miRNAs, and scRNA-seq data. Our study reveals a dynamic network involving cell-type-specific enrichment of miRNA expression patterns across diverse cell types, and dynamic miRNA target acquisition and loss in which the population of targeted mRNAs keeps pace with the dynamics of tissue development, cell diversity and lineage progression during human brain development.

Results

miRNA–mRNA interactions during brain development. To identify the landscape of miRNA–mRNA interactions occurring in the developing human brain in vivo, we performed AGO2 HITS-CLIP¹⁴ (Fig. 1). AGO2 protein-bound profiles were generated for

¹Eli and Edythe Broad Center of Regeneration Medicine and Stem Cell Research, University of California, San Francisco, San Francisco, CA, USA.

²Department of Psychiatry, University of California, San Francisco, San Francisco, CA, USA. ³Neuroscience Research Institute, University of California, Santa Barbara, Santa Barbara, CA, USA. ⁴Department of Biological Sciences and Bioengineering, Indian Institute of Technology, Kanpur, India. ⁵Department of Mechanical Engineering, University of California, Santa Barbara, Santa Barbara, CA, USA. ⁶Department of Molecular, Cellular, and Developmental Biology, University of California, Santa Barbara, Santa Barbara, CA, USA. ⁷Department of Neurology, University of California, San Francisco, San Francisco, CA, USA. ⁸New Technologies, Fluidigm Corporation, South San Francisco, CA, USA. ⁹Department of Anatomy, University of California, San Francisco, San Francisco, CA, USA. ¹⁰Department of Computer Science, University of California, Santa Barbara, Santa Barbara, CA, USA. ¹¹These authors contributed equally: T. J. Nowakowski, N. Rani, M. Golkaram, H. R. Zhou. *e-mail: tomasz.nowakowski@ucsf.edu; kosik@lifesci.ucsf.edu

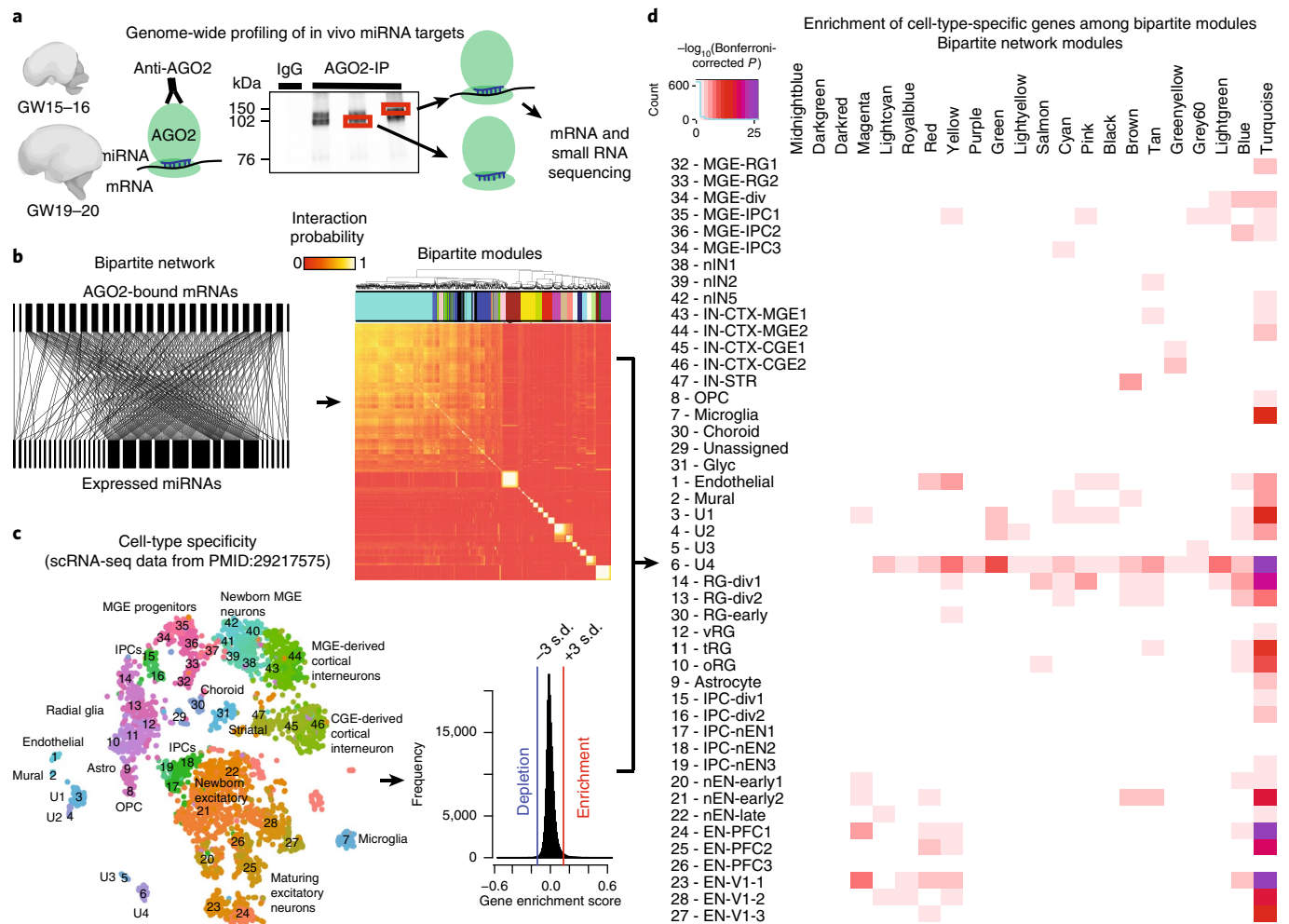


Fig. 1 | High-throughput profiling of miRNA-mRNA interactions. **a**, Experimental design. Autoradiogram of ^{32}P -labeled RNA tags cross-linked to AGO2 protein obtained from human prenatal brain homogenates. Bands at 110 kDa and 130 kDa are visible in samples with AGO2-immunoprecipitation as compared to IgG control. **b**, Complete bipartite network analysis of miRNA-mRNA interactions shown as correlation matrix, with bipartite network modules highlighted in colors above heatmap (right) and a segment of bipartite network (left) showing inhomogeneity of targeting miRNAs, relative homogeneity of targeted mRNAs and modularity of miRNA-mRNA network. **c,d**, Enrichment of bipartite modules according to cell-type identities. **(c)** Cellular specificity of genes expressed in developing human brain according to published single-cell mRNA-sequencing data set, with row names representing cell clusters described in source study²⁷, and also shown as a tSNE plot colored by cluster identity. Pearson correlation $>3\sigma$ was considered as cutoff for defining enriched or depleted genes. **(d)** Enrichment of cell-type-specific genes among bipartite network modules. Heatmap demonstrates a significant association between identified cell-types by scRNA-seq and detected modules in bipartite network. Enrichment scores represent Bonferroni-corrected $-\log_{10}(P)$ calculated using one-sided Fisher's exact test.

primary samples of the developing human brain from stages corresponding to peak neurogenesis (gestational week 15 (GW15) and GW16.5, early stage) and early gliogenesis (GW19–20.5, late stage); nine samples in total were harvested from prefrontal cortex, motor cortex area 1, visual cortex area 1 and other regions (Supplementary Table 1). AGO2-bound miRNAs and mRNAs were identified after sequencing (Fig. 1a and Supplementary Tables 1 and 2; see Methods for details). In total, 921 human miRNAs were detected and 10,505 AGO2-binding sites were identified from both protein-coding genes and noncoding genes, including long non-coding RNAs (Supplementary Table 2). About 43% of sites were in 3' untranslated regions (3' UTRs) and 27% of sites were in coding DNA sequence (CDS). For further analysis, we considered only sites identified in CDS and 3' UTRs, reflecting canonical miRNA-mRNA interactions. We identified 3,693 and 2,705 genes at early and late stages of development, respectively, that were actively targeted by miRNAs through CDS or 3' UTR parts of the transcript

(Supplementary Fig. 1). We validated a subset of the canonical AGO site interactions using luciferase reporter assays in human cells in vitro (Supplementary Fig. 1 and Supplementary Table 3). Among the detected interactions were previously validated ones, such as miRNA-9 (miR-9) with FOXG1 and HES1 mRNAs and miR-210 with CDK7 mRNA, thereby confirming the strength of the method. Unbiased enrichment analysis using the total expressed gene set in human developmental brain as background revealed that transcription factors, chromatin modifiers and signaling pathway components were enriched among miRNA targets (Supplementary Table 4). To our surprise, hundreds of the in vivo miRNA targets we identified were well-established markers of distinct cell types^{15–17}, such as regulators of neurogenesis, migration, axonogenesis, synaptogenesis and neuronal subtype specification. Broadly, single miRNAs target many mRNAs and single mRNAs are targeted by far fewer miRNAs (Supplementary Fig. 2); this represents a bipartite network of interactions between miRNAs and their direct target

mRNAs (Fig. 1b). Using a bipartite community detection algorithm¹⁸, we revealed modules of miRNA–mRNA interactions (Fig. 1b, Supplementary Figs. 2 and 3, and Supplementary Table 5; see Methods for details). Notably, the average abundance of a bound miRNA was negatively correlated with the total number of different miRNAs bound in each module (Supplementary Fig. 4). This suggests that miRNA targeting uses two strategies: (1) targeting with one or very few abundant miRNAs and (2) targeting with multiple low abundance miRNAs. To contextualize these interactions in the framework of cell diversity we projected bipartite graph modules onto cell-type-specificity information calculated from published scRNA-seq data sets (Fig. 1c,d and Supplementary Table 6). Our analysis showed marked enrichment of cell-type-specific transcripts among bipartite graph modules, suggesting that miRNAs acquire targets according to the cognate transcriptional landscape of individual cell types.

Cell-type enrichment of miRNAs. To further investigate how miRNA–mRNA interactions relate to the emerging diversity of cell types of the developing brain, we used an innovative protocol for combined detection of miRNAs and mRNAs in the same single cells (Fig. 2) using an automated microfluidic platform to perform automated cell capture, reverse transcription and targeted preamplification of mRNA and miRNA (Fig. 2a–c and Supplementary Tables 7 and 8). In addition to long-established markers of distinct cell types in the developing cortex, we selected mRNA targets according to the specificity of their expression in distinct cell types (Fig. 2b), as determined in Pollen *et al.*¹⁵. We profiled single cells isolated from human cortex samples at GW14 (deep layer neurogenesis) and GW17 (upper layer neurogenesis). To enrich for progenitor cells and newborn neurons, we microdissected samples of the cortical germinal zone, and to capture maturing neuron populations and interneurons, we microdissected cortical plate regions. In total, we retained data from 312 cells with more than ten genes detected. Clustering analysis performed based on marker gene abundance revealed 11 clusters (Supplementary Table 7). We inferred the identities of individual cell clusters as radial glia, intermediate progenitors, upper and deep cortical layer neurons, and interneurons (Fig. 2b,c). Furthermore, spatial microdissections supported further refinement of our interpretations with respect to neuronal maturation state (newborn neurons captured from the cortical germinal zone and maturing neurons captured from the cortical plate regions) (Fig. 2c). Next, for every miRNA profiled, we quantified the abundance in every cell and calculated an expression enrichment score for every cell type (Fig. 2d). To our surprise, the vast majority of miRNAs we profiled showed significant enrichment in at least one cell type, suggesting robust variation in miRNA abundance across closely related cells of the developing brain. For example, miR-221–miR-222 and miR-92a were enriched in cortical intermediate progenitor cells, in agreement with recent reports¹⁹ and consistent with their proposed roles in controlling proliferation²⁰, whereas miR-124 was enriched in postmitotic neurons, consistent with its proneural role in development²¹. Furthermore, we grouped miRNAs according to the shared pattern of abundance across single cells using weighted gene coexpression network analysis (WGCNA; Supplementary Table 8). Some of these specific miRNA coexpression modules operate within specific cell types, whereas others are broadly distributed across multiple cell types (Fig. 2e). Our analysis revealed dynamic changes in miRNA abundance in concordance with neuronal differentiation and maturation, a critical axis of transcriptional variation in the developing brain.

Dual nature of miRNA–mRNA interactions. During mouse brain development, miRNAs are involved in regulating cell-type transitions⁸, but analogous regulatory mechanisms during human brain development have largely not been investigated. To address this

limitation, we projected targets of miRNAs found to be coexpressed using single-cell quantitative PCR (sc-qPCR) (Fig. 2e) onto bipartite co-regulatory modules inferred from HITS-CLIP (Fig. 1b). This analysis revealed marked enrichment of targets of coexpressed miRNAs among bipartite network modules (Fig. 2f). Notably, we found examples of interactions in which miRNAs were enriched in neurons (WGCNA module ‘blue’, Fig. 2e), and their targets fell into a regulatory module enriched for neuronal markers (bipartite module ‘yellow’, Figs. 1d and 2f). These interactions include *DNMI1*, which encodes a GTPase involved in synaptic vesicle recycling²², and *NOVA1*, which encodes a neuron-specific RNA-binding protein²³. The presence of miRNAs and target mRNAs in the same cell type was also observed when we examined the correlation of the abundance of miRNAs and their targets across single cells (Supplementary Fig. 4b), and is consistent with the idea of cell-type-specific interactions as has been reported. For example, enrichment of miR-92 and its direct target *EOMES* in the same cell type has been reported in the developing cerebral cortex^{19,24}.

We also found interactions in which a miRNA coexpression module was enriched in neurons (WGCNA module green, Fig. 2e), but the miRNA targets show moderate enrichment for proliferating progenitors (bipartite module lightgreen, Figs. 1d and 2f). This interaction includes genes such as *H2AFZ*, which is involved in cell cycle regulation²⁵, and *PHGDH*, a radial-glia-specific gene involved in L-serine biosynthesis²⁶. In another example, miRNA coexpression module turquoise is enriched in intermediate progenitor cells (Fig. 2e), whereas the miRNA targets are enriched in bipartite modules that include neuronal and radial glia genes, and genes expressed in both (Figs. 1d and 2f). For example, *CC2D1B* is expressed highly in radial glia and neurons²⁷, and has been implicated in serotonergic signaling in neurons²⁸, but also regulates the expression of the epidermal growth factor receptor that could regulate cell proliferation²⁹.

Together, these examples highlight dynamic rewiring of miRNA–mRNA interactions during neuronal differentiation and maturation in the developing human cerebral cortex. In particular, co-modularity of miRNA–mRNA interactions as contextualized in the framework of gene and miRNA coexpression seems to follow at least two broad patterns: miRNAs are recruited in a cell type to repress genes not normally expressed in that cell type, or miRNAs are expressed in a cell type to regulate the expression of genes expressed in that same cell type. Further refinement of these dual roles may emerge from higher-resolution temporal data that synchronize single-cell developmental transitions with miRNA target degradation kinetics.

Dynamic changes in miRNA–mRNA network during development. Next, we explored the temporal axis of miRNA–mRNA interactions. We compared the abundance of miRNAs at two stages of development, GW15–16.5 and GW19–20.5 (Fig. 3), and found 69 differentially expressed miRNAs between these two stages including recently evolved miRNAs (Fig. 3a,b, Supplementary Figs. 5–11 and Supplementary Table 9). Two miRNAs, miR-449a and miR-449b-5p, which control mitotic spindle orientation during mammalian brain development^{30,31} showed the highest overall fold change in expression level between GW15–16.5 and GW19–20.5. We confirmed the expression of miR-2115, miR-449c, miR-455 and miR-362 by *in situ* hybridization (Fig. 3b and Supplementary Figs. 5–7). We also found that miRNAs miR-1286, miR-142, and miR-548aa were enriched in the occipital lobe compared to the frontal lobe (Supplementary Figs. 8–10 and Supplementary Table 2), suggesting, in agreement with recent studies³², that miRNAs may regulate regionally divergent transcriptional states in the developing human cortex.

By independently performing bipartite network analyses for samples at each of the two stages studied, we found marked preservation of most co-regulatory modules, as well as a set of distinct interactions predominantly present at one stage (Fig. 3c, Supplementary Fig. 11a and Supplementary Table 10). Notably, many of these modules

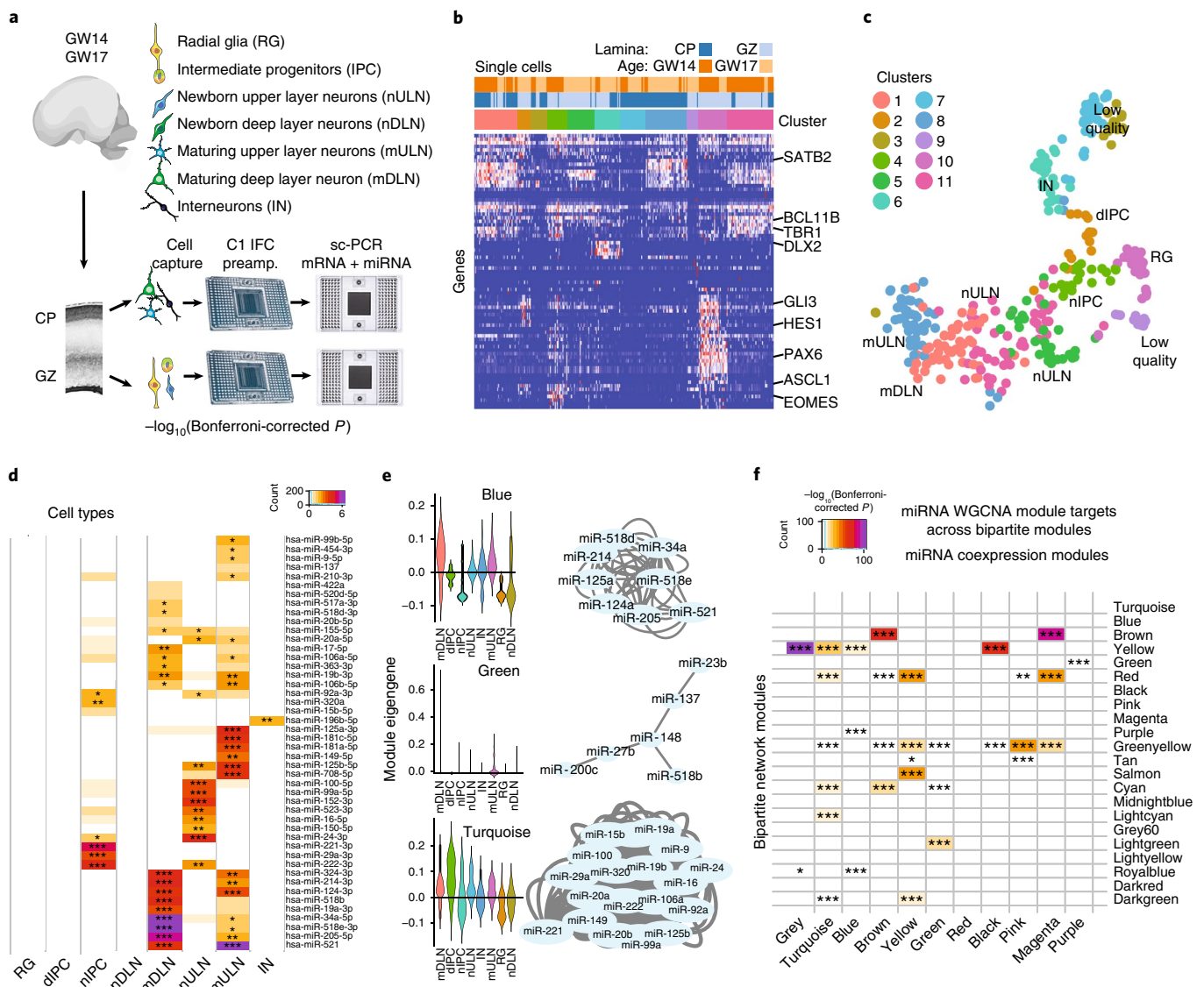


Fig. 2 | Single-cell miRNA expression profiling reveals patterns of cell-type enrichment. **a–c**, sc-qPCR profiling of mRNA and miRNA abundance in the same cell. **(a)** Schematic outlining experimental approach and cell types expected to be enriched in microdissected brain regions. C1 IFC, C1 integrated fluidic circuit; preamp., preamplification. **(b)** Heatmap of mRNA target genes used to interpret cell identities. GZ, germinal zone; CP, cortical plate. **(c)** tSNE plot of single-cell data generated using Seurat based on mRNA marker gene abundance. Colors represent unbiased clustering (see Methods for details). **d**, Heatmap representing cell-type-enriched miRNA expression profiled (one-tailed *U* test). Cell-type enrichments were calculated for cells captured from two biologically independent specimens. **e**, Weighted gene coexpression network analysis reveals modules of coexpressed miRNAs across single cells profiled in **a, b**. Network plot shows miRNAs assigned to this network based on correlation of abundance across single cells. Modules blue and turquoise are enriched in maturing deep layer neurons (mDLN) and intermediate progenitor cells (IPCs), respectively. As in **d**, this calculation was based on values from cells captured from two biologically independent specimens. dIPC, dividing intermediate progenitor cells; nIPC, nondividing intermediate progenitor cell; nULN, newborn upper layer neuron; IN, interneurons; mULN, maturing upper layer neurons; RG, radial glia; nDLN, newborn deep layer neurons. **f**, Enrichment of targets of coexpressed miRNAs across bipartite network modules. Coexpression modules were calculated for two biologically independent specimens, whereas bipartite modules were calculated for *n* = 9 biologically independent specimens. **P* < 0.05, ***P* < 0.01, ****P* < 0.001. Enrichment scores represent Bonferroni-corrected $-\log_{10}(P)$ calculated using one-sided Fisher's exact test.

were also highly preserved as compared to adult human brain interactions previously surveyed using the same experimental strategy^{32,33} (Supplementary Fig. 11b). Together, our findings suggest that miRNA-mediated regulation forms a developmentally dynamic network of interactions related to cell type, developmental stage and cortical area specificity.

Recent studies suggest that perturbations in miRNA expression may underlie human developmental neuropsychiatric disorders^{34,35}, but the specific molecular consequences remain poorly understood.

Notably, genes implicated in autism spectrum disorders (ASD) were enriched in the magenta module (Supplementary Fig. 12). In addition, we found that the expression of several miRNAs recently implicated in ASD³⁴ was biased toward expression in excitatory neurons in developing mid-gestational human samples (Supplementary Fig. 12), although their expression patterns may change over the course of brain development³⁶. Genes targeted by miR-137 in the developing brain differ greatly from targets identified in adult human brain tissue³³, suggesting that in vivo target interactions of these

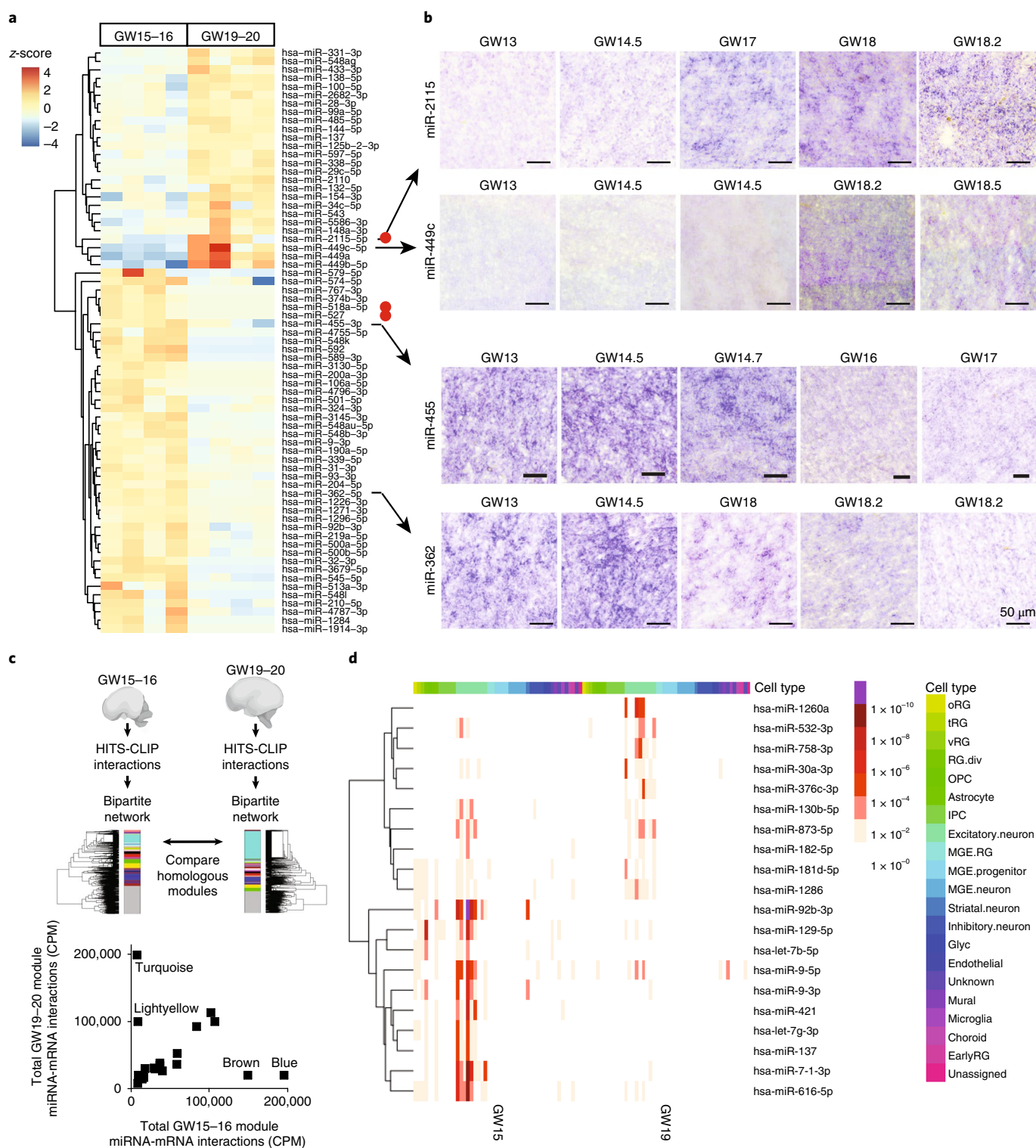


Fig. 3 | Dynamic changes in miRNA regulatory networks during development. **a**, Differential expression analysis identifies miRNAs differentially expressed between GW15-16 and GW19-20 developing human cortex. Red dots indicate primate-specific miRNAs. Heatmap displays expression z-score of each miRNA in that sample. Each column represents a specimen, and specimens are arranged according to age. **b**, Validation of differentially expressed miRNAs by in situ hybridization in developing human neocortex sections. Images show staining in outer subventricular zone. For every specimen, the experiment was repeated three times in different sections with similar results. **c**, Module preservation analysis for networks generated across GW15-16 and across GW19-20 samples as well as a set of distinct interactions present predominantly at one stage (for example, association of modules turquoise and lightyellow with GW19-20 and modules brown and blue with GW15-16). GW15-16 module names are used to compare GW15-16 modules with their homologs in GW19-20. CPM, count per million. **d**, Stage-specific changes in miRNA targets according to their specificity to distinct cell types of developing brain identified using single-cell RNA-seq²⁷. Heatmap shows enrichment P value of miRNAs in distinct cell types in each stage of development.

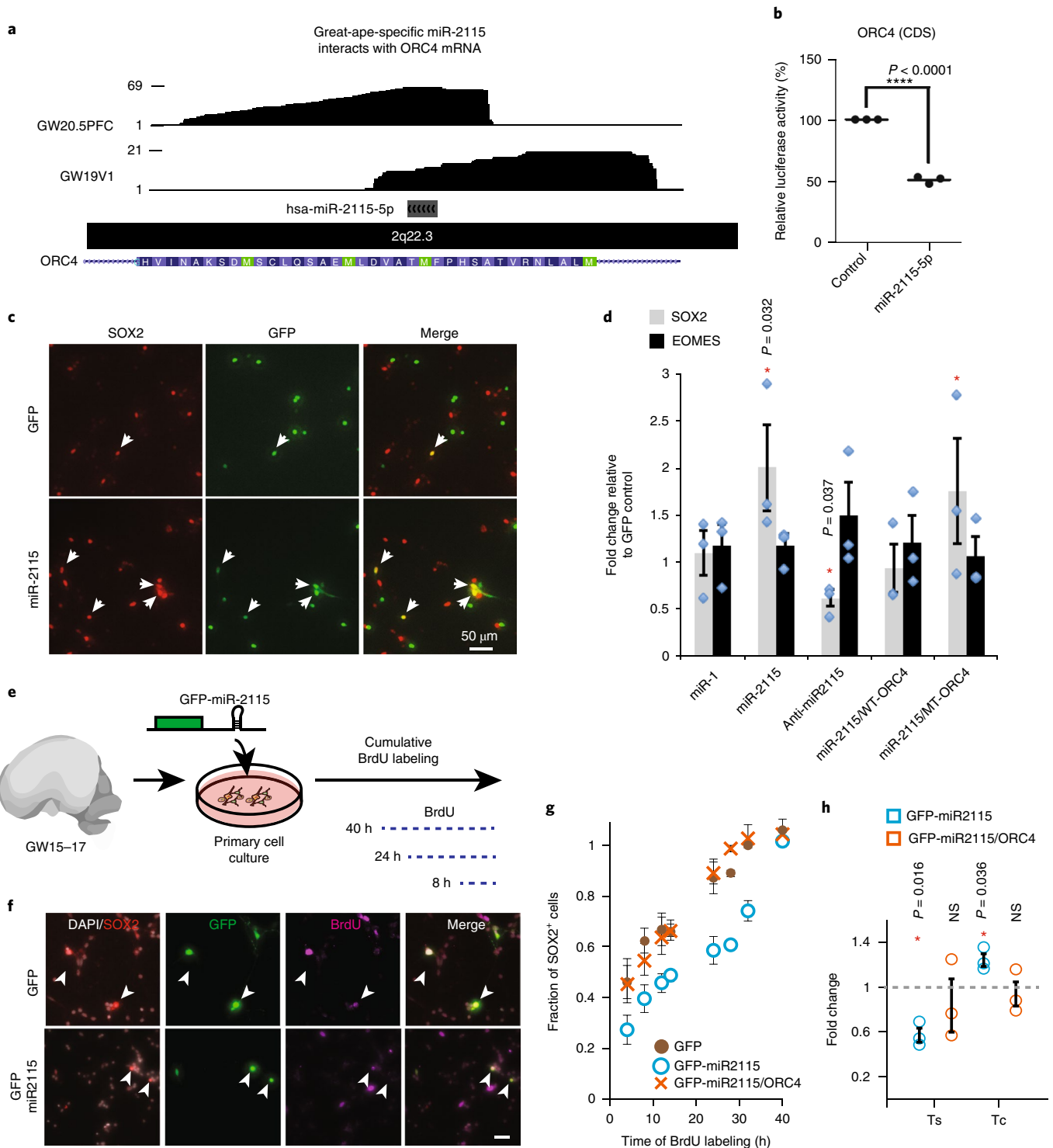


Fig. 4 | miRNAs contribute to cell-type-specific function. **a**, HITS-CLIP data tracks showing reads spanning a predicted miR-2115 response element in the CDS of ORC4 mRNA. **b**, Luciferase reporter assay demonstrating functionality of miR-2115 interaction through CDS site identified in **a** (**** $P < 0.0001$, unpaired two-sided t test), $n = 3$ biologically independent experiments. Center value represents mean and error bars represent s.e.m. **c**, **d**, miR-2115 influences radial glia development. **(c)** Primary radial glia were transfected with miR-2115 expression plasmid and cultures were immunostained for markers of radial glia (SOX2) and intermediate progenitors (EOMES). **(d)** Quantification of immunopositive cells ($n = 3$ biological replicates). miR-1, GFP-miR1 small RNA overexpression control construct; miR-2115, GFP-miR2115 overexpression construct; anti-miR-2115, miR-2115 inhibitor co-transfected with GFP expression construct. All constructs and reagents are described in Methods. * $P < 0.05$, two-sided Student's t test. Center values represent mean and error bars represent s.e.m. **e**, Experimental design of cumulative BrdU labeling in human cells in vitro performed to assess impact of miR-2115 on progenitor proliferation. **f**, Immunostaining of human cultured cells. Arrowheads indicate GFP*SOX2⁺ cells. Scale bar, 25 μm . **g**, **h**, Quantification of BrdU labeling of SOX2⁺ cells **(g)** and estimates of S-phase length (Ts) and cell cycle length (Tc) **(h)**. Center values represent mean and error bars represent s.e.m. In **h**, values are relative to control conditions ($n = 3$ specimens). * $P < 0.05$, two-sided Student's t test.

miRNAs may also change substantially during development (Supplementary Table 11).

To explore this observation more broadly, we considered whether individual miRNAs dynamically change their target landscape during development. We examined the intersection of cell-type specificity of miRNA targets at either stage of development (GW15–16 and GW19–20) and found miRNAs whose targets are enriched in one cell type during early development, and in a different cell type later in development (Fig. 3d). We found many miRNAs, such as miR-181d-5p, miR-129-5p, miR-9 and miR-616-5p, whose targets were enriched in different cell types in early developmental stages and late developmental stages, indicating changing roles for these miRNAs during brain development. miR-1260a, miR-758-3p, and miR-376c-3p targets were enriched in excitatory neurons only in late stages. miR-376c-3p is of interest because it can significantly enhance neural differentiation of in vitro pluripotent stem cell models³⁷. Targets of miRNAs miR-92b-3p, let-7-5p, miR-421, and miR-137 were enriched for radial glial markers or excitatory neurons only at early stages. Both miR-92b-3p and miR-130b-5p are specifically associated with neural progenitors¹³. These examples further underscore the dynamic remodeling of miRNA interaction networks during development and suggest that further analysis of these interactions may reveal previously unappreciated cellular vulnerabilities of miRNA–mRNA interactions to disease mutations. Understanding cell-type-specific miRNA expression profiles and the respective miRNA targets may help identify cellular patterns of selective vulnerability to disorders affecting miRNA expression by highlighting gene regulatory networks that might be perturbed in disease states.

miR-2115 regulates cell cycle in human radial glia. The developmental transition between GW15–16.5 and GW19–20.5 coincides with changes in proliferation rates of radial glia and depletion of proliferative capacity in the human ventricular zone³⁸. Among the top five miRNAs differentially expressed between these stages, a great-ape-specific miRNA, miR-2115, was prominently upregulated at GW19–20 in the germinal zones (Fig. 3a,b and Supplementary Figs. 5 and 7). Among miR-2115 targets, *ORC4*, a known regulator of DNA replication³⁹, was enriched in radial glia at early stages of development^{15,17}, and is a member of the turquoise module, which is enriched for GW19–20.5 HITS-CLIP interactions within a segment corresponding to a putative miR-2115 response element (Fig. 3c and Supplementary Table 11). Mutations in *ORC4* are linked to Meier–Gorlin syndrome, which is frequently associated with microcephaly, suggesting that this gene may have an important role in normal brain development⁴⁰. We hypothesized that miR-2115 acts through a radial-glia-enriched gene regulatory network involving *ORC4* to regulate cell cycle dynamics and thereby influences cortical progenitor cell function. To test this hypothesis, we first confirmed the binding of the *ORC4* miRNA response element and miR-2115 using a reporter assay and inhibitor studies (Fig. 4a–d and Supplementary Fig. 1) as well as a nearly zero *P* value using the stringent target prediction algorithm PACCMIT-CDS⁴¹. Next, we overexpressed a synthetic miRNA, mmu-miR-2115 (see Methods), in developing mouse cortex and found a greater proportion of radial glia, but a lower proportion of radial glia in mitosis, among the cells electroporated with mmu-miR-2115as compared to control electroporation (Supplementary Fig. 13). Similarly, manipulation of miR-2115 expression influenced the development of human primary radial glia cells in vitro. Both overexpression and inhibition of miR-2115 changed the proportion of cells expressing SOX2, indicating a possible role for this miRNA in proliferation or differentiation (Fig. 4c,d and Supplementary Fig. 13b). The phenotype was rescued by the addition of wild-type *ORC4* reporter construct expressed together with miR-2115 (Fig. 4d).

To more specifically test for a possible cell cycle phenotype, we performed a cumulative bromodeoxyuridine (BrdU) incorporation

assay (Fig. 4e–g) in human radial glia using GFP–miR2115 construct. The change in cell cycle rate caused by miR-2115 overexpression was rescued by addition of *ORC4* protein expression construct (full-length) (Fig. 4h). This showed that miR-2115 expression regulates normal cell cycle duration in human radial glia by controlling *ORC4* protein levels. Together, these findings suggest that miR-2115 emerged recently in evolution and integrated into post-transcriptional regulatory networks controlling cell cycle dynamics during human cortical development.

Discussion

Our study reveals several distinct mechanisms by which miRNA regulatory pathways contribute to human brain development. We developed a new single-cell-profiling approach for combined mRNA and miRNA profiling in the same cell. Using this approach, we examined cell-type-specific patterns of miRNA abundance, which revealed highly dynamic changes in miRNA expression, even among the closely related cells of the developing brain. Our findings support the emerging view that many miRNAs are expressed in cell-type-specific patterns^{42,43}.

To gain insight into miRNA–mRNA interactome remodeling during cell-type transitions, we combined high-throughput profiling of miRNA–mRNA interactions with cell-type-specific gene expression profiles. Many miRNAs, including those expressed in multiple cell types, regulate the expression of cell-type-specific genes. Dynamic changes in cellular transcriptomes occurring during developmental lineage progression are probably controlled through a variety of regulatory networks involving transcription factors, signaling pathways, and post-transcriptional, epigenetic and epitranscriptomic mechanisms. Our analysis further emphasizes the contribution of miRNAs to the vast majority of such networks, including genes regulating excitatory neuron laminar and projection fates, such as regulators of callosal projection neurons (*BHLHE22* and *SATB2*; ref. 44), corticothalamic neurons (*TBRI*; ref. 45) and interneurons (*LHX6* and *DLX5*; ref. 46). Understanding the implications of these interactions for neuronal subtype specification will require highly multiplexed approaches for functional validation.

Furthermore, by projecting cell-type-specific miRNA and mRNA expression patterns against the modular framework of the bipartite network of miRNA–mRNA interactions, our study reveals dynamic developmental remodeling of miRNA–mRNA interaction networks involving conserved and recently evolved miRNAs, as well as cell-type-specific miRNA regulatory networks in the developing human brain (Supplementary Table 12). Comprehensive understanding of cell-type-specific miRNA–mRNA interactions may reveal previously unappreciated patterns of the selective vulnerability of cell types in neurodevelopmental disorders, including ASDs.

This multimodal approach to cell-type identity reveals an additional regulatory element introduced into radial glial cells. The expression of a great-ape-specific miRNA (miR-2115) targets *ORC4*, a gene involved in cell division. Because the target site is located in the conserved CDS, it does not have the same need for coevolution as the presumably less-constrained 3' UTR, indicating that this regulatory interaction would be more likely to evolve. Functional sites have been extensively reported in the CDS^{47–50} and photoactivatable ribonucleoside-enhanced crosslinking and immunoprecipitation (PAR-CLIP) experiments in humans show that the numbers of CDS and 3' UTRs are similar⁴⁸, a finding supported by predictive algorithms⁴⁹. The functional data here on the control of cell cycle duration in radial glia are consistent with the microcephalic primordial dwarfism phenotype of Meier–Gorlin syndrome due to mutations in *ORC4*. These individuals have lissencephaly and hypoplastic frontal lobes among other structural abnormalities.

In addition to specific miRNA coexpression modules associated with specific cell types (Fig. 2e), many miRNAs are expressed in many cell types, and they are likely regulated by different trans-factors,

depending on cell-type-specific transcriptomes. In these latter cases, some miRNA modules can be broadly distributed across multiple cell types (Fig. 2e). These latter modules may represent shared functionalities across different cell types or poorly resolved intermediate states. Setting boundaries for cell clusters is a statistical matter that can accrue additional support with more miRNA expression data. miRNA abundance is not easily measured with commonly used single-cell RNA-sequencing platforms. With more highly resolved single-cell quantification, novel cell identities may become apparent or cell type boundaries may emerge as less bistable and instead depend on an analog model.

The developing primate cerebral cortex forms a tiered structure that contains an astonishing diversity of cell types. These diverse cell identities emerge during early development from highly dynamic progenitor cells, which undergo sequential changes in cellular transcriptome while simultaneously generating daughter cells that differentiate into one of dozens of terminal cell identities. Mitosis is a pivotal event in which both daughter cells have to decide to reenter the cell cycle or differentiate. Upon differentiation, fate specification and refinement are controlled by a suite of transcription factors. Post-transcriptional regulation of their expression by miRNAs acts a network-level control mechanism that can serve as a critical tuner of precise and robust identities. We found that groups of miRNAs can assume cell-type-specific patterns of expression and can regulate hundreds of cell-type-specific transcripts. Postmitotic cells undergo sequential changes in gene expression as they migrate to their architectonic destinations, and they often alter their states in response to environmental cues before establishing terminal identities. Notably, the dynamic process of cell-type maturation must use miRNAs differently than stably differentiated cells, in which the prominent role of miRNAs is homeostatic to buffer change. This strategic difference in the role of miRNAs—to foster change rather than stability—suggests further realms of cellular systems control over cell identity.

Online content

Any methods, additional references, Nature Research reporting summaries, source data, statements of data availability and associated accession codes are available at <https://doi.org/10.1038/s41593-018-0265-3>.

Received: 5 December 2017; Accepted: 2 October 2018;

Published online: 19 November 2018

References

- Tasic, B. Single cell transcriptomics in neuroscience: cell classification and beyond. *Curr. Opin. Neurobiol.* **50**, 242–249 (2018).
- Griffiths, J. A., Scialdone, A. & Marioni, J. C. Using single-cell genomics to understand developmental processes and cell fate decisions. *Mol. Syst. Biol.* **14**, e8046 (2018).
- Tanay, A. & Regev, A. Scaling single-cell genomics from phenomenology to mechanism. *Nature* **541**, 331–338 (2017).
- Zeng, H. & Sanes, J. R. Neuronal cell-type classification: challenges, opportunities and the path forward. *Nat. Rev. Neurosci.* **18**, 530–546 (2017).
- Kosik, K. S. MicroRNAs and cellular phenotypy. *Cell* **143**, 21–26 (2010).
- Monticelli, S. et al. MicroRNA profiling of the murine hematopoietic system. *Genome Biol.* **6**, R71 (2005).
- Fineberg, S. K., Kosik, K. S. & Davidson, B. L. MicroRNAs potentiate neural development. *Neuron* **64**, 303–309 (2009).
- Volvert, M. L., Rogister, F., Moonen, G., Malgrange, B. & Nguyen, L. MicroRNAs tune cerebral cortical neurogenesis. *Cell Death Differ.* **19**, 1573–1581 (2012).
- Berezikov, E. et al. Phylogenetic shadowing and computational identification of human microRNA genes. *Cell* **120**, 21–24 (2005).
- Kapsimali, M. et al. MicroRNAs show a wide diversity of expression profiles in the developing and mature central nervous system. *Genome Biol.* **8**, R173 (2007).
- Baudet, M. L. et al. miR-124 acts through CoREST to control onset of Sema3A sensitivity in navigating retinal growth cones. *Nat. Neurosci.* **15**, 29–38 (2011).
- Bernstein, E. et al. Dicer is essential for mouse development. *Nat. Genet.* **35**, 215–217 (2003).
- Jonsson, M. E. et al. Comprehensive analysis of microRNA expression in regionalized human neural progenitor cells reveals microRNA-10 as a caudalizing factor. *Development* **142**, 3166–3177 (2015).
- Moore, M. J. et al. Mapping Argonaute and conventional RNA-binding protein interactions with RNA at single-nucleotide resolution using HITS-CLIP and CIMS analysis. *Nat. Protoc.* **9**, 263–293 (2014).
- Pollen, A. A. et al. Molecular identity of human outer radial glia during cortical development. *Cell* **163**, 55–67 (2015).
- Camp, J. G. et al. Human cerebral organoids recapitulate gene expression programs of fetal neocortex development. *Proc. Natl. Acad. Sci. USA* **112**, 15672–15677 (2015).
- Miller, J. A. et al. Transcriptional landscape of the prenatal human brain. *Nature* **508**, 199–206 (2014).
- Liu, X. & Murata, T. Community detection in large-scale bipartite networks. *Information and Media Technologies* **5**, 184–192 (2010).
- Florio, M. et al. Human-specific gene ARHGAP11B promotes basal progenitor amplification and neocortex expansion. *Science* **347**, 1465–1470 (2015).
- Yu, B. et al. miR-221 and miR-222 promote Schwann cell proliferation and migration by targeting LASS2 after sciatic nerve injury. *J. Cell. Sci.* **125**, 2675–2683 (2012).
- Maiorano, N. A. & Mallamaci, A. Promotion of embryonic cortico-cerebral neurogenesis by miR-124. *Neural Develop.* **4**, 40 (2009).
- Boumil, R. M. et al. A missense mutation in a highly conserved alternate exon of dynamin-1 causes epilepsy in fitful mice. *PLoS Genet.* **6**, <https://doi.org/10.1371/journal.pgen.1001046> (2010).
- Buckanovich, R. J., Yang, Y. Y. & Darnell, R. B. The onconeural antigen Nova-1 is a neuron-specific RNA-binding protein, the activity of which is inhibited by paraneoplastic antibodies. *J. Neurosci.* **16**, 1114–1122 (1996).
- Nowakowski, T. J. et al. MicroRNA-92b regulates the development of intermediate cortical progenitors in embryonic mouse brain. *Proc. Natl. Acad. Sci. USA* **110**, 7056–7061 (2013).
- Magri, L. et al. c-Myc-dependent transcriptional regulation of cell cycle and nucleosomal histones during oligodendrocyte differentiation. *Neuroscience* **276**, 72–86 (2014).
- Kawakami, Y. et al. Impaired neurogenesis in embryonic spinal cord of Phgdh knockout mice, a serine deficiency disorder model. *Neurosci. Res.* **63**, 184–193 (2009).
- Nowakowski, T. J. et al. Spatiotemporal gene expression trajectories reveal developmental hierarchies of the human cortex. *Science* **358**, 1318–1323 (2017).
- Hadjighassem, M. R. et al. Human Freud-2/CC2D1B: a novel repressor of postsynaptic serotonin-1A receptor expression. *Biol. Psychiatry* **66**, 214–222 (2009).
- Deshar, R., Cho, E. B., Yoon, S. K. & Yoon, J. B. CC2D1A and CC2D1B regulate degradation and signaling of EGFR and TLR4. *Biochem. Biophys. Res. Commun.* **480**, 280–287 (2016).
- Fededa, J. P. et al. MicroRNA-34/449 controls mitotic spindle orientation during mammalian cortex development. *EMBO J.* **35**, 2386–2398 (2016).
- Wu, J. et al. Two miRNA clusters, miR-34b/c and miR-449, are essential for normal brain development, motile ciliogenesis, and spermatogenesis. *Proc. Natl. Acad. Sci. USA* **111**, E2851–E2857 (2014).
- Sousa, A. M. M. et al. Molecular and cellular reorganization of neural circuits in the human lineage. *Science* **358**, 1027–1032 (2017).
- Boudreau, R. L. et al. Transcriptome-wide discovery of microRNA binding sites in human brain. *Neuron* **81**, 294–305 (2014).
- Wu, Y. E., Parikhshak, N. N., Belgard, T. G. & Geschwind, D. H. Genome-wide, integrative analysis implicates microRNA dysregulation in autism spectrum disorder. *Nat. Neurosci.* **19**, 1463–1476 (2016).
- Abu-Elneel, K. et al. Heterogeneous dysregulation of microRNAs across the autism spectrum. *Neurogenetics* **9**, 153–161 (2008).
- He, M. et al. Cell-type-based analysis of microRNA profiles in the mouse brain. *Neuron* **73**, 35–48 (2012).
- Liu, J. et al. A reciprocal antagonism between miR-376c and TGF-beta signaling regulates neural differentiation of human pluripotent stem cells. *FASEB J.* **28**, 4642–4656 (2014).
- Nowakowski, T. J., Pollen, A. A., Sandoval-Espinosa, C. & Kriegstein, A. R. Transformation of the radial glia scaffold demarcates two stages of human cerebral cortex development. *Neuron* **91**, 1219–1227 (2016).
- Guernsey, D. L. et al. Mutations in origin recognition complex gene ORC4 cause Meier-Gorlin syndrome. *Nat. Genet.* **43**, 360–364 (2011).
- de Munnik, S. A. et al. Meier-Gorlin syndrome: growth and secondary sexual development of a microcephalic primordial dwarfism disorder. *Am. J. Med. Genet. A* **158A**, 2733–2742 (2012).
- Marin, R. M., Sulc, M. & Vanicek, J. Searching the coding region for microRNA targets. *RNA* **19**, 467–474 (2013).
- Ramachandran Iyer, E. P. et al. Barcoded oligonucleotides ligated on RNA amplified for multiplex and parallel in-situ analyses. Preprint at *bioRxiv* <https://doi.org/10.1101/281121> (2018).

43. Faridani, O. R. et al. Single-cell sequencing of the small-RNA transcriptome. *Nat. Biotechnol.* **34**, 1264–1266 (2016).
44. Srinivasan, K. et al. A network of genetic repression and derepression specifies projection fates in the developing neocortex. *Proc. Natl. Acad. Sci. USA* **109**, 19071–19078 (2012).
45. Hevner, R. F. et al. Tbr1 regulates differentiation of the preplate and layer 6. *Neuron* **29**, 353–366 (2001).
46. Marin, O., Anderson, S. A. & Rubenstein, J. L. Origin and molecular specification of striatal interneurons. *J. Neurosci.* **20**, 6063–6076 (2000).
47. Forman, J. J., Legesse-Miller, A. & Collier, H. A. A search for conserved sequences in coding regions reveals that the let-7 microRNA targets Dicer within its coding sequence. *Proc. Natl. Acad. Sci. USA* **105**, 14879–14884 (2008).
48. Hafner, M. et al. Transcriptome-wide identification of RNA-binding protein and microRNA target sites by PAR-CLIP. *Cell* **141**, 129–141 (2010).
49. Schnall-Levin, M., Zhao, Y., Perrimon, N. & Berger, B. Conserved microRNA targeting in *Drosophila* is as widespread in coding regions as in 3' UTRs. *Proc. Natl. Acad. Sci. USA* **107**, 15751–15756 (2010).
50. Schnall-Levin, M. et al. Unusually effective microRNA targeting within repeat-rich coding regions of mammalian mRNAs. *Genome Res.* **21**, 1395–1403 (2011).

Acknowledgements

The authors thank S. Wang, C. Sandoval-Espinosa, E. Guzman, A. Bhaduri and N. Li for providing research resources, technical help and helpful comments during manuscript preparation. N.R. acknowledges support (Ramanujan Fellowship SB/S2/RJN-030/2017)

from Science and Engineering Research Board, Department of Science & Technology, India. This research was supported by the Dr. Miriam and Sheldon G. Adelson Medical Research Foundation (K.S.K.) and National Institutes of Health (NIH) awards U54NS100717 (K.S.K.), MH105989 (A.R.K.) and R01NS075998 (A.R.K.). This work was supported by a grant from the Simons Foundation (SFARI 491371; T.J.N.).

Author contributions

K.S.K., N.R., T.J.N., H.R.Z., L.R.P. and A.R.K. designed and supervised the study. J.A.W., A.L. and B.A. designed and optimized single-cell miRNA and mRNA PCR protocol. B.A., N.R., T.J.N., A.A.P. and B.A. performed experiments. H.R.Z., M.G., K.H., B.A., N.R. and T.J.N. performed data analysis. T.J.N., N.R. and K.S.K. wrote the paper with contribution from all authors.

Competing interests

The authors declare no competing interests.

Additional information

Supplementary information is available for this paper at <https://doi.org/10.1038/s41593-018-0265-3>.

Reprints and permissions information is available at www.nature.com/reprints.

Correspondence and requests for materials should be addressed to T.J.N. or K.S.K.

Publisher's note: Springer Nature remains neutral with regard to jurisdictional claims in published maps and institutional affiliations.

© The Author(s), under exclusive licence to Springer Nature America, Inc. 2018

Methods

Dissociation cell culture. Cortical cells were dissociated using papain (Worthington Biochemical) and cultured on tissue culture plates coated with matrigel (BD Biosciences). Cells were plated at about 100,000–200,000 cells per well of a 12-well plate. Culture medium used in this experiment consisted of DMEM (Invitrogen, 11965) supplemented with N2 (Invitrogen, 12587-010), B27 (17502-048), penicillin and streptomycin, but without serum. At the time of plating, culture medium was spiked with recombinant human fibroblast growth factor (FGF) (10 ng mL⁻¹, Peprotech, AF-100-18B). About 24–48 h after plating, cells were transfected with plasmids using Lipofectamine 2000 (Life Technologies) according to the manufacturer's protocol. BrdU (Sigma) was diluted in the culture medium for dissociated cells (DMEM, supplemented with B27 and N2, with penicillin and streptomycin) at 50 µg mL⁻¹.

Sample collection. All mice in this study were obtained from Simonsen Laboratories and maintained according to protocols approved by the Institutional Animal Care and Use Committee at University of California, San Francisco (UCSF). De-identified human tissue samples were collected with subject consent in strict observance of the legal and institutional ethical regulations for elective pregnancy termination. Protocols were approved by the Human Gamete, Embryo and Stem Cell Research Committee (UCSF Institutional Review Board). Sample processing for dissociation, fixation, cryosectioning and long-term storage was performed as described¹⁵.

In utero electroporation. Survival in utero surgery was performed in strict observance of protocols and recommendations approved by the Institutional Animal Care and Use Committee at UCSF. Plasmids were injected at ~1.5 µg µL⁻¹ as described^{24,51}. Although the ORC4 protein sequence is highly conserved, the miR-2115-5p miRNA recognition element (MRE) sequence is not fully conserved in mouse. We generated a mutant miR-2115-5p hairpin sequence (mmu-miR-2115) whose seed would be complementary to the mouse ORC4 mRNA coding sequence at the site homologous to the human miR-2115-5p MRE.

Plasmid constructs. gBlocks gene fragments for the respective target sites or miRNAs (Supplementary Table 3) with restriction site(s) at their ends were purchased from IDT. Restriction site cloning was performed using the standard method. Full-length ORC4 expression plasmid was generated using gene synthesis using a full-length human ORC4 and cloned into CAG-IRES-GFP vector using the GeneArt service (Thermo Fisher).

Luciferase activity assay. Luciferase activity assay was performed as described⁵² in HEK293 cells. The target sites were cloned in psiCHECK2 (Promega) plasmid (Supplementary Table 3), and miR-2115 and miR-9 were cloned in pCAG-GFP (Addgene 11150) plasmid (Supplementary Table 2). miRNA mimics (Life Technologies) were used for other miRNA assays. For ORC4, wild-type MRE reporter was named WT-ORC4, and a reporter lacking the miR2115 MRE was called MT-ORC4.

Fluorescence reporter expression measurement. Fluorescence reporters were generated by cloning the respective target site, as indicated above, into the NotI site of the GFP expression vector (Addgene, plasmid 11153), and validated by Sanger sequencing. For each culture condition, 100 ng of plasmid was transfected into primary dissociated human cells in culture, alone or together with LNA anti-miRNA inhibitor (Qiagen) (50 pmol). Mutant reporters were generated as gBlocks from IDT lacking the miRNA response element being tested. After 72 h in culture, cells were lightly fixed in 4% paraformaldehyde, followed by imaging of fluorescence using SP5 confocal microscope at constant laser power and detector conditions. About ten fields of view were considered at random, and all cells in every field of view were used to quantify the average intensity of fluorescence signal (per pixel) across four conditions for every miRNA–mRNA interaction examined: control reporter with wild-type MRE, control reporter with wild-type MRE together with anti-miRNA inhibitor, reporter lacking an MRE, and reporter lacking an MRE together with anti-miRNA inhibitor. For wild-type and mutant reporter, we calculated the ratio of average fluorescence per pixel with and without anti-miR inhibitor. The experiment was repeated for cells derived from three independent biological specimens ($n = 3$, at GW14, GW18 and GW20), except for miR-2115-ORC4 CDS interactions, which were tested in three additional biological specimens (GW15, GW17 and GW19). For experiments presented in Supplementary Fig. 1g, loading control CAG-dsRed expression plasmid (100 ng) was co-transfected with the reporter to increase the accuracy of our quantification efforts. dsRed immunofluorescence was to normalize the GFP fluorescence signal in every cell analyzed.

In situ hybridization. In situ hybridization in primary tissue sections was performed as described⁵³, except that we did not perform a probe linearization step. Digoxigenin-conjugated probes for miRNA detection were purchased from Exiqon or Qiagen.

Immunofluorescence. Thin 20-µm cryosections were collected on superfrost slides (VWR) using Leica CM3050S cryostat. Immunohistochemistry-based

detection of specific antigens was performed according to standard protocols. In short, heat-mediated antigen retrieval was performed in 10 mM sodium citrate for 15 min. Cells were permeabilized in PBS (pH = 7.4) supplemented with 2% Triton X-100. Blocking buffer consisted of PBS supplemented with 10% donkey serum, 0.2% gelatin and 2% Triton X-100. The antibodies used in this study included chicken anti-GFP (1:1,000, Aves Labs GFP-1020), rabbit anti-PAX6 (1:300, Covance prb-278p), and mouse anti-pHH3 (1:100, Abcam ab1791). These antibodies have been used previously in human tissue⁵⁴. Secondary antibodies were obtained from Life Technologies. Nuclei were counterstained with 4,6-diamidino-2-phenylindole (DAPI, Sigma).

After cell fixation, BrdU epitope was unmasked using 2 N hydrochloric acid, neutralized using 0.1 M boric acid, and stained using a rat antibody to BrdU (BU1/75, ICR1; 1:50, Abcam ab6326). This antibody has been used previously in human tissue⁵⁵. Coverslips were mounted with Aqua-mount (Lerner Laboratories).

Images were collected with a Leica DMI 4000B microscope using a Leica DFC295 camera and Leica TCS SP5 X confocal microscope. Quantification of immunopositive cells was performed in Adobe Photoshop. Mouse embryonic electroporation cortical staining was quantified as described²⁴. Quantification results for every biological replicate (embryo) represent an average of quantification across three nonadjacent sections. Replicates were drawn from at least two independent litters. Quantification of BrdU incorporation into SOX2⁺ primary cells in culture was performed by imaging randomly selected fields in the well using tile-scanning feature. GFP⁺ were first evaluated for expression of SOX2, and after that BrdU immunoreactivity was assessed. Some 100–200 SOX2⁺GFP⁺ cells were evaluated per well. Quantification of cell cycle phenotypes was performed by fitting linear regression, and cell cycle parameters were calculated as described⁵⁵.

AGO2-HITS-CLIP. We chose AGO2 as a target for HITS-CLIP experiments as most other studies did for miRNA target identification because among the Argonaute family of proteins, AGO2 has slicer activity, which is not the case for AGO1, AGO3 or AGO4 in mammals^{56,57}. This mechanism of mRNA destruction by miRNA binding is both prevalent and implements a more rapid and more readily detectable effect on downstream pathways. Moreover, we chose AGO2 because the data would be suitable for comparison with the previously generated HITS-CLIP data in the adult brain³³, which we analyzed to gain insights into the preservation of the miRNA–mRNA interaction modules in Supplementary Fig. 11b. The experiments were performed as described¹⁴ except for a few modifications. Monoclonal antibody to Ago2 (Sigma, 11A9 clone, SAB4200085) was used to perform immunoprecipitation of protein on protein G dynabeads (Invitrogen, 100-03D). For the negative control, goat anti-rat IgG antibody (Sigma, A9037) was used. RNase dilution of 1:50,000 was used after optimization. Primary tissue samples at stages corresponding to peak neurogenesis (GW15–16.5) upper layer neurogenesis and early gliogenesis were analyzed. Sample quality and data processing metrics were comparable to published results for adult human brain HITS-CLIP study³³. Some 3,258 genes were actively targeted by miRNAs through protein coding (CDS) or 3' UTRs of the transcript. Notably, ~80% of gene targets were detected in at least two samples, suggesting that we recovered the majority of in vivo mRNA targets.

Library preparation for sequencing RNA tags on Ion Torrent. For library preparation, all steps were performed as described¹⁴, except that the primers with adapter sequences were modified according to the Ion Torrent sequencing platform.

Primers with adapter sequences were 5'-CCATCTCATCCCTGCGTGTCTCCGACTCAGAGGGAGGACGATGCGG-3' and 5'-CCTCTCTATGGGCGAGTCGGTGATCCGCTGGAAGTGACTGACAC-3'. The bands corresponding to AGO2–miRNA–target complexes (130 kDa) were cut. miRNA libraries and target mRNA libraries were made separately.

Single-cell quantitative PCR analysis. Capture of single cells was done using the C1 Single-Cell Auto Prep Integrated Fluidic Circuit (Fluidigm Corporation), which uses a microfluidic chip to capture the cells and perform lysis, reverse transcription and cDNA amplification in nanoliter reaction volumes of miRNA and mRNA species at the same time. The details of the cell capture protocol used are described in protocol 100-6667 at <http://www.fluidigm.com/>. During the reverse transcription step, miRNAs are reverse transcribed to cDNA using stem loop reverse transcription (RT) primers from the Megaplex RT primer pool (Life Technologies) that are specific for mature miRNA species and reagents from the Single-Cell-to-CT kit (Life Technologies). mRNA species were reverse-transcribed at the same time during this process using mRNA primers present in the Single-Cell VILO RT mix. Megaplex primers and mRNA primers were added at the recommended concentrations. The choice of sc-qPCR miRNA targets was constrained by the pool of miRNA pre-enrichment primers from Life Technologies, and by the cost of Taqman primers. Therefore, the decision to include a primer for particular miRNA was driven by a combination of expression analysis and literature search. In particular, we leveraged published expression profiling data from developing human or nonhuman primate brain tissue^{33,58–61}.

During the PCR step, products were uniformly amplified from cDNA templates using Megaplex PreAmp Primers (Life Technologies), a pool of DELTAgene primers and Single-Cell Preamp mix from the Ambion Single-Cell-to-CT kit (Life Technologies).

Cycling conditions were as followed: for reverse transcription, primers were annealed at 16 °C for 2 min, followed by extension at 42 °C for 1 min and extension at 50 °C for 1 min. This cycle was repeated 40 times, followed by a hold step at 85 °C for 5 min. For preamplification, polymerase was activated at 95 °C for 10 min, followed by incubation at 55 °C for 2 min and 72 °C for 2 min. Preamplification cycling steps were performed by denaturing step at 95 °C for 15 min followed by extension at 60 °C for 4 min. At the end, the reaction was incubated at 99.9 °C for 10 min, and the reaction was cooled to 4 °C.

After preamplification PCR, the amplicons were diluted at 1:4 with C1 DNA Dilution reagent (Fluidigm 100-5317) and stored in –20 °C until needed. qPCR was carried out using the 96.96 dynamic array (Fluidigm) according to the manufacturer's protocol (100-3909 and 100-9792). Gene expression analysis was done using Fluidigm Real-Time PCR Analysis software (version 3.0.2). Cycle threshold (Ct) values were obtained and then square root normalized to stabilize the variance.

Clustering of single cells was performed using a recently developed method combining Louvain clustering of single-cell sample coordinates with Jaccard distance metric⁶². Principal components analysis (PCA) dimensionality reduction and clustering was performed in the space of the following genes meaningful for cell type classification: *CORO1C*, *FAM107A*, *GLI3*, *CLU*, *CENPF*, *PROM1*, *NEX*, *C3*, *SATB2*, *ALDOA*, *AUTS2*, *EOMES*, *TBR1*, *SOW10*, *MOXD1*, *CSF3R*, *TAGLN3*, *SEMA3C*, *ELAVL2*, *GRIA2*, *CLDN11*, *TJP1*, *PDGFD*, *PPP1R17*, *DDAH1*, *TGFBR1*, *NOVA1*, *BCL11B*, *GAD1*, *OLIG1*, *NEUROG2*, *NEUROD6*, *ETV5*, *DLX2*, *RBF31*, *CNTNAP2*, *PALLD*, *MKI67*, *PAX6*, *GFAP*, *ADRA2A*, *FBXO32*, *GPX3*, *KIF26B*, *SLC1A3*, *PARD6A*, *VIM*, *PARD3*, *CBX1*, *DLL1*, *CNN3*, *NR4A2*, *TFAP2C*, *SOX2*, *PDGFRA*, *PTPRZ1*, *MEF2C*, *DLX5*, *FGF12*, *ERBB4*, *ASPM*, *OLIG2*, *BTG2*, *TNC*, *TUBB3*, *ASCL1*, *ROBO2*, *HES1*, *HES5*, *SLA*, *SOX5*, and *DLX6-AS1*. T-stochastic neighbor embedding (tSNE) was used to visualize cells in two dimensions.

Computational analyses. Preprocessing and mapping of AGO2-HITS-CLIP tags. Barcodes were identified and reads were separated into each sample. Adapter sequences at both ends of reads were removed using Cutadapt⁶³. Trimmed reads were mapped to the human genome (hg19) with novoalign (<http://www.novocraft.com/>). Identical alignments were collapsed in each sample to remove PCR replicates. Strand-specific read coverage was then calculated using the alignments from each sample.

miRNA profiling and differential expression analysis. Adapter-trimmed AGO2 reads from miRNA libraries were mapped to human miRNA precursors from miRBase version 21 using miRdeep2 (ref. ⁶⁴). DESeq2 was used to identify differentially expressed miRNAs between two developmental stages⁶⁵.

Peak calling and identification of clusters and AGO footprint. Piranha and zero-truncated negative binomial model (ZTNB) were used to calculate the significance of read coverage at each mapped genomic position in each sample^{33,66}. In summary, the read heights for each mapped genomic position were assumed to be sampled from an underlying ZTNB distribution, and parameters for ZTNB probability density functions were estimated using read height measured at all positions of the genome. *P* values were calculated as the probability of observing a read height as large as the height in question and assigned to each position. We used Fisher's method to calculate the joined *P* values at each genomic position across all samples. Positions with a joined false discovery rate (FDR) < 5% were deemed significant. Significant positions within 50 nucleotides (nt) of one another were merged into a single contiguous interval as a single AGO-binding site, and resulting regions of < 50 nt were symmetrically extended to 50 nt to account for the AGO-binding footprint⁶⁷. AGO-binding sites were then annotated according to their overlapping gene structures from GENCODE annotation version 19.

Identification of miRNAs for each AGO-binding site. To identify miRNAs that bind each AGO site on mRNAs and long noncoding RNAs, all types of canonical binding sites including 7mer-1A, 7mer-m8 and 8mer⁶⁸ for all prenatal brain-expressed miRNAs were searched within the full-length AGO-binding sites defined as above. miRNAs with MREs within each AGO-binding site were counted.

WGCNA analysis. To detect groups of coexpressed miRNAs, we used the WGCNA R package⁶⁹. Cells analyzed using sc-qPCR were included in this analysis. To intersect miRNA coexpression module targets with bipartite network annotations (Fig. 2f), for every miRNA coexpression module we took the union of HITS-CLIP predicted targets of the miRNAs in that module.

Cell-type specificity and enrichment analysis for miRNAs in single-cell data. We performed a one-tailed Wilcoxon–Mann–Whitney *U* test to detect differential enrichment of each miRNA in each cell type versus the other cell types. A miRNA was defined to be enriched in a cell type, if it was significantly more highly

expressed in that cell type compared to the other cells in that population (adjusted *P* < 0.05).

Correlation with target mRNA levels. To correlate the relative abundance of coexpressed miRNAs and their targets across the major cell types of the developing brain, we calculated the average module eigengene for modules detected in Supplementary Fig. 2 across radial glia, intermediate progenitors, neurons and interneurons. In parallel, we used published scRNA-seq data³⁸ and the cell-type assignments therein for radial glia, interneurons, intermediate progenitors and excitatory cortical neurons to calculate cell-type-specific average expression level of the genes identified as AGO2-bound miRNA targets and nontargets. We then correlated the average module eigengene with all of the gene targets predicted by HITS-CLIP and nontargets, and we calculated the average correlation for each in Fig. 2f. To compare the average correlations, we first converted correlation to *z*-scores using Fisher transformation. The differences between average *z*-scores (for targets and nontargets) were divided by the joint standard errors and significance was calculated based on normal distribution.

Gene enrichment analysis. Transcriptome data from similar prenatal brain tissues⁷⁰ was downloaded and expressed genes were used as a better background set for gene enrichment analysis. The *P* value was calculated with a hypergeometric test and adjusted using the Benjamini–Hochberg method (unless otherwise mentioned). To formally demonstrate that cell-type-specific genes are regulated by miRNAs, we used published scRNA-seq data sets to calculate cell-type-specificity scores using ideal vector correlation for every miRNA target identified by HITS-CLIP (Supplementary Table 7). We defined a gene to be a signature of a cell type if its Pearson correlation was 3 σ higher than the mean Pearson correlation score of all genes in all cell types (histogram in Fig. 1c)^{15,27}.

To calculate the overlap with ASD genes, we used genes associated with ASD annotated by SFARI Gene⁷¹. A module was defined to be enriched in ASD if the FDR corrected *P* value of hypergeometric test was < 0.05 (the total number of expressed genes in prenatal brain tissues was also used as the background).

Bipartite community detection analysis. An unweighted (binary) bipartite network was constructed such that there exists an edge between each miRNA–mRNA pair if and only if such interaction is detected by AGO2-HITS-CLIP. First, this network was shown to be scale-free (*P* < 0.001), and then by generating random networks while constraining the number of edges and nodes to the original miRNA–mRNA network and calculating Barber's modularity score⁷² (null distribution), the miRNA–mRNA network was shown to be significantly modular (*P* < 2 × 10^{–16} for permutation test). Label propagation followed by the bipartite recursively induced modularity algorithm (LP-BRIM)¹⁸ was used for community detection in this bipartite network. Due to the stochasticity of this method, we obtained robust communities by repeating LP-BRIM 2,500 times and determining the overlap among all the iterations.

Bipartite network construction. The bipartite networks were generated using all detected target genes (3,463 nodes in mode I) and all miRNA (514 nodes in mode II). An edge exists between only one node in mode I and one node in mode II if such interaction is present in the HITS-CLIP data set (Supplementary Table 2) (no edge is allowed between nodes in mode I (or mode II)). Hence in this study, three distinct networks were built using GW15–16, GW19–20 and the combined GW15–16 and GW19–20 HITS-CLIP data set with 31,859, 20,734, and 36,176 total edges, respectively.

Bipartite network modularity statistics. First, the R bipartite package⁷³ was used to show that the constructed network was scale-free. For consistency with the literature definition of scale-free networks, we showed that this network significantly obeyed power law, truncated power law and exponential distribution (Supplementary Fig. 11a,b, *P* < 0.001). Next, to demonstrate that these networks were significantly modular, we first generated a null distribution by randomly shuffling the edges between the nodes and calculating Barber's modularity score. Finally, we showed that the network was significantly modular using a permutation test (*P* < 2 × 10^{–16}).

Bipartite community detection. We used R lpbrim package⁷⁴ to detect communities in the described networks. Due to stochasticity of the method, we ran the community detection algorithm 25 times and obtained the best solution among all 25 runs (with maximum Barber's modularity score). We repeated this procedure 100 times and found consensus clustering as follows.

We first defined the overlap rate matrix (ORM) as a symmetric *n* by *n* matrix where *n* is the total number of miRNA and target genes combined. Each entry ORM_{*i*} shows the probability (or rate) of which target gene (or miRNA) *i* lies within the same cluster as target gene (or miRNA) *j* upon 100 runs.

The obtained ORM was further clustered using hierarchical clustering (Supplementary Fig. 11c,d). Each obtained diagonal block after hierarchical clustering represents one community (containing both target genes and miRNAs that have significant intramodular interactions compared to their intermodular interactions with target genes (or miRNAs) in other communities).

Finally, dynamic branch cutting implemented in the dynamicTreeCut R package was used for tree cutting and assigning cluster identification numbers to each node (Supplementary Fig. 11e,f).

We repeated this procedure to show that the obtained clusters are robust and reproducible (Supplementary Fig. 11c,d).

Bipartite module preservation analysis. To determine whether each identified module in the GW15–16 network was statistically preserved in GW19–20, we first found the closest module in GW19–20 to GW15–16 in terms of the number of shared nodes in that module. Then, using the hypergeometric test, module preservation statistics were obtained and corrected using the Benjamini–Hochberg method for multiple comparison. As shown in Fig. 3f, two homolog modules in GW15–16 and GW19–20 had similar interaction levels, suggesting preserved topology of modules as well. Names of GW15–16 module colors were used to label Fig. 3f.

Inference of evolutionary history of miR-2115. To infer the evolutionary history of miR2115, we used genome sequences obtained from the University of California Santa Cruz (UCSC) Genome Browser (using the most recent genome assemblies). Alignments were done using the Geneious bioinformatics platform (version 9.1.8). Human *SPINK8* gene sequence was annotated with introns, exons, CDS and UTR regions and miR-2115 location according to National Center for Biotechnology Information RefSeq track on the UCSC Genome Browser. *SPINK8* gene orthologs were located in chimpanzee, gorilla, orangutan and gibbon genomes using the Other RefSeq track on UCSC Genome Browser. We excluded Bonobo because of the poor quality of genome assembly at the area of interest. Primate *SPINK8* sequences were aligned with human *SPINK8* sequences individually using the MUSCLE Alignment algorithm. Primate *SPINK8* sequences were annotated with introns, exons, CDS and UTR regions and miR-2115 location according to alignment with the annotated human *SPINK8* sequence. Originally primate *SPINK8* genes were annotated according to the Other RefSeq track on UCSC Genome Browser but this yielded varied and unreliable results. The presence or absence of miR-2115 was determined based on alignment of human miR-2115 to the orthologous primate sequence (with mature transcript and seed region taken into consideration). Annotated human, chimpanzee, gorilla, orangutan, and gibbon *SPINK8* intron 3/4 sequences, where intron miR-2115 is located, were aligned together to visualize changes in intron sequences between species. Boundaries of insertions and deletions in *SPINK8* intron 3/4 occurring between species were defined based on evolutionarily chronological alignments of *SPINK8* intron 3/4 sequences (for example, gibbon and orangutan alignment, orangutan and gorilla alignment, and so on). Evolution of the *SPINK8* intron 3/4 was predicted using the fewest mutations that would give rise to observed insertions and deletions.

Statistics. Statistical tests, sample sizes and assumptions are indicated in each corresponding figure legend, except for bipartite network analysis, which is described above. Data distribution was assumed to be normal but this was not formally tested.

Across all experiments and quantification, each tissue specimen was considered a biological replicate. Although we did not use formal methods of randomization, quantification of immunostaining was always performed blind, such that identity of sample and condition was not known to the person performing the quantification.

Across all experiments, specimens with low viability of cells after plating, specimens contaminated with bacteria, or specimens for which we could not perform the entire experiment were not included in the analysis and not reported. For mouse embryos, we selected embryos with highest quality of electroporation based on visual assessment under a stereotaxic fluorescence microscope. For animal and human embryonic tissue experiments, we did not examine the embryos for sex.

No statistical methods were used to predetermine sample sizes but our sample sizes are similar to those reported earlier³³. Across all experiments, data distribution was assumed to be normal but this was not formally tested.

Reporting Summary. Further information on research design is available in the Nature Research Reporting Summary linked to this article.

Code availability. Scripts used in data analysis for this manuscript can be found at GitHub: <https://github.com/mgolkaram/Nature-Neuroscience-2018-miRNA-mRNA-paper>.

Data availability

The data used in this study are available as part of the publicly available Gene Expression Omnibus database under accession number [GSE107468](https://www.ncbi.nlm.nih.gov/geo/query/acc.cgi?acc=GSE107468).

References

- Saito, T. In vivo electroporation in the embryonic mouse central nervous system. *Nat. Protoc.* **1**, 1552–1558 (2006).
- Rani, N. et al. A primate lncRNA mediates notch signaling during neuronal development by sequestering miRNA. *Neuron* **90**, 1174–1188 (2016).
- Pollen, A. A. et al. Low-coverage single-cell mRNA sequencing reveals cellular heterogeneity and activated signaling pathways in developing cerebral cortex. *Nat. Biotechnol.* **32**, 1053–1058 (2014).
- Hansen, D. V. et al. Non-epithelial stem cells and cortical interneuron production in the human ganglionic eminences. *Nat. Neurosci.* **16**, 1576–1587 (2013).
- Takahashi, T., Nowakowski, R. S. & Caviness, V. S. Jr. The cell cycle of the pseudostratified ventricular epithelium of the embryonic murine cerebral wall. *J. Neurosci.* **15**, 6046–6057 (1995).
- Meister, G. et al. Human Argonaute2 mediates RNA cleavage targeted by miRNAs and siRNAs. *Mol. Cell* **15**, 185–197 (2004).
- Liu, J. et al. Argonaute2 is the catalytic engine of mammalian RNAi. *Science* **305**, 1437–1441 (2004).
- Moreau, M. P., Bruse, S. E., Jornsten, R., Liu, Y. & Brzustowicz, L. M. Chronological changes in microRNA expression in the developing human brain. *PLoS One* **8**, e60480 (2013).
- Berezikov, E. et al. Diversity of microRNAs in human and chimpanzee brain. *Nat. Genet.* **38**, 1375–1377 (2006).
- Somel, M. et al. MicroRNA-driven developmental remodeling in the brain distinguishes humans from other primates. *PLoS Biol.* **9**, e1001214 (2011).
- Arcila, M. L. et al. Novel primate miRNAs coevolved with ancient target genes in germinal zone-specific expression patterns. *Neuron* **81**, 1255–1262 (2014).
- Shekhar, K. et al. Comprehensive classification of retinal bipolar neurons by single-cell transcriptomics. *Cell* **166**, 1308–1323 e1330 (2016).
- Martin, M. Cutadapt removes adapter sequences from high-throughput sequencing reads. *EMBnet J.* **17**, 10–12 (2011).
- Friedländer, M. R., Mackowiak, S. D., Li, N., Chen, W. & Rajewsky, N. miRDeep2 accurately identifies known and hundreds of novel microRNA genes in seven animal clades. *Nucleic Acids Res.* **40**, 37–52 (2011).
- Love, M. I., Huber, W. & Anders, S. Moderated estimation of fold change and dispersion for RNA-seq data with DESeq2. *Genome Biol.* **15**, 550 (2014).
- Uren, P. J. et al. Site identification in high-throughput RNA–protein interaction data. *Bioinformatics* **28**, 3013–3020 (2012).
- Chi, S. W., Zang, J. B., Mele, A. & Darnell, R. B. Ago HITS-CLIP decodes miRNA–mRNA interaction maps. *Nature* **460**, 479 (2009).
- Lewis, B. P., Burge, C. B. & Bartel, D. P. Conserved seed pairing, often flanked by adenosines, indicates that thousands of human genes are microRNA targets. *Cell* **120**, 15–20 (2005).
- Langfelder, P. & Horvath, S. WGCNA: an R package for weighted correlation network analysis. *BMC Bioinformatics* **9**, 559 (2008).
- Liu, S. J. et al. Single-cell analysis of long non-coding RNAs in the developing human neocortex. *Genome Biol.* **17**, 67 (2016).
- Banerjee-Basu, S. & Packer, A. SFARI Gene: an evolving database for the autism research community. *Dis. Models Mech.* **3**, 133–135 (2010).
- Barber, M. J. Modularity and community detection in bipartite networks. *Phys. Rev. E* **76**, 066102 (2007).
- Dormann, C. F., Gruber, B. & Fründ, J. Introducing the bipartite package: analysing ecological networks. *Interaction* **1**, 0.2413793 (2008).
- Seal, A. & Wild, D. J. Netpredictor: R and Shiny package to perform drug–target network analysis and prediction of missing links. *BMC Bioinformatics* **19**, 265 (2018).

Reporting Summary

Nature Research wishes to improve the reproducibility of the work that we publish. This form provides structure for consistency and transparency in reporting. For further information on Nature Research policies, see [Authors & Referees](#) and the [Editorial Policy Checklist](#).

Statistical parameters

When statistical analyses are reported, confirm that the following items are present in the relevant location (e.g. figure legend, table legend, main text, or Methods section).

n/a | Confirmed

- The exact sample size (n) for each experimental group/condition, given as a discrete number and unit of measurement
- An indication of whether measurements were taken from distinct samples or whether the same sample was measured repeatedly
- The statistical test(s) used AND whether they are one- or two-sided
Only common tests should be described solely by name; describe more complex techniques in the Methods section.
- A description of all covariates tested
- A description of any assumptions or corrections, such as tests of normality and adjustment for multiple comparisons
- A full description of the statistics including central tendency (e.g. means) or other basic estimates (e.g. regression coefficient) AND variation (e.g. standard deviation) or associated estimates of uncertainty (e.g. confidence intervals)
- For null hypothesis testing, the test statistic (e.g. F , t , r) with confidence intervals, effect sizes, degrees of freedom and P value noted
Give P values as exact values whenever suitable.
- For Bayesian analysis, information on the choice of priors and Markov chain Monte Carlo settings
- For hierarchical and complex designs, identification of the appropriate level for tests and full reporting of outcomes
- Estimates of effect sizes (e.g. Cohen's d , Pearson's r), indicating how they were calculated
- Clearly defined error bars
State explicitly what error bars represent (e.g. SD, SE, CI)

Our web collection on [statistics for biologists](#) may be useful.

Software and code

Policy information about [availability of computer code](#)

Data collection

Data analysis

For manuscripts utilizing custom algorithms or software that are central to the research but not yet described in published literature, software must be made available to editors/reviewers upon request. We strongly encourage code deposition in a community repository (e.g. GitHub). See the Nature Research [guidelines for submitting code & software](#) for further information.

Data

Policy information about [availability of data](#)

All manuscripts must include a [data availability statement](#). This statement should provide the following information, where applicable:

- Accession codes, unique identifiers, or web links for publicly available datasets
- A list of figures that have associated raw data
- A description of any restrictions on data availability

Field-specific reporting

Please select the best fit for your research. If you are not sure, read the appropriate sections before making your selection.

Life sciences Behavioural & social sciences Ecological, evolutionary & environmental sciences

For a reference copy of the document with all sections, see [nature.com/authors/policies/ReportingSummary-flat.pdf](https://www.nature.com/authors/policies/ReportingSummary-flat.pdf)

Life sciences study design

All studies must disclose on these points even when the disclosure is negative.

Sample size	We generated data based on the availability of primary tissue samples. In total we processed 9 primary tissue samples for AGO2-clip, and used saturation analysis to determine that this number was effective in recovering the majority of targeted genes.
Data exclusions	For single cell qPCR we excluded any assay that did not give positive value after 30 cycles of amplification in at least two single cells. We removed cells with positive signal from at least 5 assays.
Replication	We used strict measures to highlight high confidence AGO2 binding clusters in the mRNA. Firstly, we used multiple biological replicates for each age-range of specimens and curated the dataset to the list of target sites detected in at least two biological specimens. For all other experiments that were carried out, all attempts at replication were successful.
Randomization	Samples were randomized due to the random collection of primary tissue specimens and were processed in random order. Sc-qPCR data was generated and processed in random order.
Blinding	Sample collection was performed by researchers at UCSF, the samples were processed for AGO2-CLIP at UCSB without cross-referencing with sample metadata. For single cell qPCR, data was processed in parallel and only analyzed together following a melting curve analysis. miR2115 overexpression analysis and brdU analysis experiment was performed by blinding the experimental conditions for brdu/sox2 quantification

Reporting for specific materials, systems and methods

Materials & experimental systems

n/a	Included in the study
<input checked="" type="checkbox"/>	<input type="checkbox"/> Unique biological materials
<input checked="" type="checkbox"/>	<input type="checkbox"/> Antibodies
<input type="checkbox"/>	<input checked="" type="checkbox"/> Eukaryotic cell lines
<input checked="" type="checkbox"/>	<input type="checkbox"/> Palaeontology
<input type="checkbox"/>	<input checked="" type="checkbox"/> Animals and other organisms
<input checked="" type="checkbox"/>	<input type="checkbox"/> Human research participants

Methods

n/a	Included in the study
<input checked="" type="checkbox"/>	<input type="checkbox"/> ChIP-seq
<input checked="" type="checkbox"/>	<input type="checkbox"/> Flow cytometry
<input checked="" type="checkbox"/>	<input type="checkbox"/> MRI-based neuroimaging

Eukaryotic cell lines

Policy information about [cell lines](#)

Cell line source(s)	HEK293 cells were obtained from a commercial source.
Authentication	This cell line was never authenticated
Mycoplasma contamination	We have not tested this line for mycoplasma contamination
Commonly misidentified lines (See ICLAC register)	We used the HEK293 cell line and there was no particular reason for choosing it, other than that it is commonly used in the lab for luciferase experiments.

Animals and other organisms

Policy information about [studies involving animals](#); [ARRIVE guidelines](#) recommended for reporting animal research

Laboratory animals	We have pregnant dams Swiss-Webster in this experiment, but only analyzed embryonic animals. We never test embryos for sex. therefore we expect approximately even representation of males and females. We used three pregnant dams in this
--------------------	---

experiments. Because Simonsen does not inform us about the age of these animals, we do not know what ages they are. The embryos used in the analysis were at E15.5 stage of development. However, we did not confirm the age by Theiler criteria, and the age is only based on the plug check information provided by Simonsen.

Wild animals

this study did not involve wild animals

Field-collected samples

this study did not involve field-collected animals